

Complex layered deformation within the Aegean crust and mantle revealed by seismic anisotropy

Brigitte Endrun¹, Sergei Lebedev², Thomas Meier³, Céline Tirel²,
Wolfgang Friederich⁴

Supplementary Information

Supplementary Methods

1. Anisotropic Rayleigh wave tomography: details and validation

Recent array analyses of surface waves have provided increasingly detailed information on mantle deformation by mapping the distribution of azimuthal seismic anisotropy with depth and its lateral variations^{33–39,51–54}. A small anisotropic perturbation to phase velocity C can be expressed by

$$\delta C(\omega, \Psi) = C_1(\omega) + C_2(\omega) \cos(2\Psi) + C_3(\omega) \sin(2\Psi) + C_4(\omega) \cos(4\Psi) + C_5(\omega) \sin(4\Psi), \quad (1)$$

with ω denoting angular frequency and Ψ indicating the azimuth of the horizontal wave vector^{55,56}.

The coefficients C_{1-5} are depth integral functions containing the unperturbed Rayleigh wave displacement eigenfunctions and combinations of the 21 different components of the general anisotropic elasticity tensor.

Calculations for mineralogical and petrological upper mantle models show that Rayleigh-wave 4Ψ terms can be expected to be very small^{31,57}. We included the 4Ψ terms in our analysis,

¹Institute of Earth and Environmental Sciences, University Potsdam, Karl-Liebknecht-Str. 24, 14476 Potsdam, Germany

²Dublin Institute for Advanced Studies, Geophysics Section, 5 Merrion Square, Dublin 2, Ireland

³Institute of Geosciences, Christian-Albrechts-University Kiel, Otto-Hahn-Platz 1, 24118 Kiel, Germany

⁴Institute of Geology, Mineralogy and Geophysics, Ruhr-University Bochum, 44780 Bochum, Germany

however, and verified that our results and conclusions are not sensitive to their presence and amplitude in tomographic solutions.

a) Data

Seismograms from 872 globally distributed earthquakes (Supplementary Fig. 1) were used to measure Rayleigh wave dispersion along 129 raypaths between 36 broad-band stations from different Aegean networks⁴⁰. The path coverages at the 15 and 30 s periods are very similar (Supplementary Fig. 2). Robust phase-velocity curves for each of the paths were averaged from numerous one-event interstation measurements^{2,40,58}. By using a large number of events from different epicentral areas (i.e. source directions and distances), we aim to decrease the influence of great circle deviations and non-plane waves generated outside the area between the two stations⁵⁹. For each event, segments of the calculated phase-velocity curves were carefully selected based on visual inspection of the phase-velocity curves and the time-frequency representation of the waveforms². The main selection criteria are that the curves are smooth and do not deviate unrealistically far from the average. Curves from the two opposite along-arc directions were considered separately for each station pair to check for any visible multipathing effects. No clear differences between the two propagation directions were found for any of the station pairs.

Anomalous propagation of Rayleigh waves has been observed previously for raypaths across Crete, i.e. along the southern forearc^{2,40}, where the subducting African slab lies at a shallow depth and influences ray propagation up to high frequencies. Observed phase velocities appear biased towards greater values for arc-parallel paths in this region. We do not show or interpret azimuthal anisotropy along the forearc, though, as this area is not well resolved by our data set. Any anomalous propagation for arc-parallel raypaths in this region thus should not affect our results or conclusions.

In order to test the influence of the small-scale roughness seen on our measured phase-

velocity curves, we performed tomographic inversions both using the original curves and using slightly smoothed versions of them. The smoothed curves were obtained in undamped inversions for best-fitting path-specific 1D models using the Neighbourhood Algorithm^{40,60} and fit the measured data closely, while, also, being free from the small-scale roughness (noise) (Supplementary Fig. 3). The results of the tomographic inversions of both the measured and the smoothed curves are similar, and our conclusions regarding large-scale anisotropy in the Aegean hold regardless of which version of the data is used. In the figures presented in this paper, we show results of the inversion of the curves slightly smoothed using the Neighbourhood Algorithm. Supplementary Fig. 3 shows examples of phase-velocity curves measured along paths that are highlighted in Supplementary Fig. 2 and sample crust of different thicknesses. Strong variations in crustal thickness have been found in previous surface wave studies of the Aegean^{61–65} and have also been confirmed by P- and S-wave tomography^{48,49,66,67}, seismic reflection and refraction profiles^{68,69}, receiver functions^{47,70,71} and inversion of gravity data¹².

b) Resolution tests

The variance reduction achieved in the tomographic inversions – using the optimal smoothing parameters determined by resolution tests (e.g. Supplementary Figures 4 and 5) – is consistently larger than 75% at periods up to 25 s and over 65% at 30 s. All of the measurements are explained by the tomographic models within 20 m/s or within the actual estimated standard errors, whichever is smaller. The spatial coherence of the “ 2Ψ ” anisotropic orientations computed with and without the “ 4Ψ ” terms allowed to vary indicates the robustness of the anisotropy results and shows any potential trade-off between 2Ψ and 4Ψ anisotropic terms (Supplementary Fig. 6). The spatial coherence is a measure of variations in both orientation and amplitude of two vector datasets that has been used previously to compare modeled and measured orientations of anisotropy⁷² or to compare results of anisotropic tomography for different damping parameters⁵². Here it is calculated for angular shifts between -90° and $+90^\circ$, using an uncer-

tainty (width of the resulting peak) of 10° . The nearly-Gaussian shapes of the resulting curves (Supplementary Fig. 6) indicate an overall coherence between the pairs of the datasets, with the position of the main peaks showing only small angles of rotation. This means that the result for 2Ψ anisotropic orientations depends only weakly on whether 4Ψ terms are included in the inversion or not. The anisotropic 4Ψ terms themselves are small in the central part of the regions where raypath density would allow to resolve them (Supplementary Fig. 7).

Further evidence for negligible trade-off between the isotropic and anisotropic (2Ψ and 4Ψ) anomalies is given by Supplementary Fig. 8, which shows a comparison between the isotropic and anisotropic results for periods 15 s and 30 s for three different inversion runs: one allowing only for isotropic perturbations, one including isotropic perturbations and 2Ψ anisotropy and finally one additionally allowing for 4Ψ anisotropy. Isotropic anomalies show similar amplitudes and patterns for each run, except at the southern boundary of the covered area around Crete, where resolution is low. This area is not included in our interpretation. Orientations and amplitudes of anisotropy are also consistent, especially in the northern Aegean, whether 4Ψ terms are included or not. Anisotropy in the southernmost part of the region is less robust for periods around 30 s, but anisotropy in the south-central Aegean (Cyclades) is still well resolved and low at 30 s. This means that the patterns we are discussing and interpreting in the main paper are robust. Finally, trade-offs between isotropic and anisotropic anomalies can also be estimated from Supplementary Fig. 5 (and similar calculations at different periods). For example, at 15 s, the average amplitude of spurious anisotropy introduced in the well resolved area (see Fig. 2) when using the optimum smoothing parameter is 0.5%, indicating that the mapping of isotropic anomalies into anisotropy is significantly smaller than the anisotropic anomalies resolved and interpreted.

The stability of the results was checked when excluding some percentage (from 10% to 50%) of the worst-fit measurements from the dataset. For the results in Fig. 2, the pattern in 2Ψ anomalies as measured by the spatial coherence^{52,72} is stable when the dataset is reduced by up

to 20%. At 15 s, the anisotropy pattern is stable even when only half of the data is used.

A strict resolution test with the input anisotropy pattern being the observed one rotated by 90 degrees³⁸ confirms that the data coverage is sufficient to resolve the anisotropic anomalies reliably (Supplementary Fig. 9). Results of this test can also be used to estimate the uncertainty in the measured anisotropy orientation and magnitude, as the tomographic inversion does not supply any formal errors for these values. Considering only the well-resolved parts of the area (as shown in Fig. 2), the mean deviations in anisotropy orientation are 7° at 15 s and 14° at 30 s, while median values are 3° and 4°, respectively. Mean deviations in anisotropy amplitude are 27% at 15 s and 33% at 30 s, with median values of 22% and 31%. From this, we conclude that uncertainty is slightly higher at longer periods, but is below 15° in anisotropy orientation and around 30% in anisotropy amplitude for the results presented.

2. Inversion for Vs structure and anisotropy

Supplementary Fig. 10 shows Fréchet derivatives of the phase velocity of the fundamental Rayleigh mode with respect to S-wave velocities, at 15 and 30 s periods. The main features of the velocity model used (i.e. Moho depth and existence of a water layer) are similar to the average situation in the Aegean, as determined by seismic^{40,47–49,61–71} and gravity data¹². The Fréchet derivatives show that, apart from the very shallow structure, the depth level that influences the phase velocities most is the lower crust (10–25 km depth) for a period of 15 s and the uppermost mantle around 45 km depth for a period of 30 s. To further verify that the difference in the distributions of phase-velocity anisotropy between 12–18 s period on the one hand and 25–30 s period on the other hand (Fig. 2) really reflects a change in anisotropy in the lower crust compared to the uppermost mantle, we inverted the anisotropic phase velocity maps for average azimuthally anisotropic Vs profiles in the northern and south-central Aegean. The two regions are defined as North of 39° N and East of 22° E for the northern Aegean and as located between 36° N and 37.5° N and East of 23° E for the south-central Aegean.

Firstly, the isotropic perturbations derived from tomography are averaged over each of the regions for each period between 10 s and 30 s for the northern Aegean and 10 s and 100 s for the south-central Aegean, respectively, and added to the average reference velocity value of each period. The extension to longer periods is possible for the south-central Aegean region as this area is covered mainly by STS-2 sensors with 120 s eigenperiod, while the coverage of the other regions is achieved by shorter-period instruments⁴⁰. Thus, two average isotropic reference curves are derived. These curves are inverted for isotropic shear-wave velocity models by an iterative, gradient-search inversion^{2,58} as shown in Supplementary Fig. 11 (a, b). The resulting Moho depths agree with seismological observations^{40,64,69,71} as well as gravity data¹² which consistently show a nearly constant Moho depth around 30 km in the northern Aegean, while the Moho in the south-central Aegean lies shallower, between 20 and 25 km. While the mantle velocities of the average isotropic northern Aegean model are fairly constant, as far as resolvable, the average isotropic model for the south-central Aegean shows increasing velocities from approximately 80 km depth, relating to the subducting African lithosphere. Reduced velocities in the layer above might hint at the shallow asthenosphere in the south-central Aegean, which has been more clearly observed along individual raypaths⁴⁰ and agrees with other observations of low velocities^{66,67} and strong attenuation^{73,74} around 60 km depth beneath the southern Aegean and the volcanic arc.

To invert for azimuthal anisotropy with depth, the azimuthal phase velocity anisotropy was averaged across each region for each period, similar to the isotropic data. Then, the projection of this average phase velocity anisotropy on azimuths between -90° and $+90^\circ$ was calculated in 5° steps for each period. For each of these azimuths, the anisotropic perturbations, calculated as described above, were added to the average isotropic curve for the region and also inverted for shear-wave velocity with depth^{2,58}. The same parameterisation as in the inversion of the average isotropic curve was used, but the result of the isotropic inversion was used as starting model and the Moho depth was kept fixed. The inversion for each azimuth used in the projection

was independent from all other inversions. Supplementary Fig. 11 (c,d) shows the perturbations of the resulting models, colour-coded according to azimuth, relative to the starting models. The highest amount of shear-wave anisotropy is found in the crust for the south-central Aegean and in the uppermost mantle for the northern Aegean. The largest values of shear-wave velocity are observed at azimuths of around 40° in the south-central Aegean crust and around 5° in the northern Aegean upper mantle (Supplementary Fig. 11).

The inversions for V_s anisotropy as described above relies on assumptions on the relationship of phase velocities to elastic parameters. Specifically, phase velocity was computed from V_s profiles assuming that isotropic relationships are valid. This assumption and its effects were discussed previously by a number of authors. Recently, ref. 75 has investigated this question and computed the differences between phase velocities derived under assumptions of isotropic and anisotropic models, for the same anisotropy distributions. For the fundamental mode, in particular, as used in the present study, the differences turned out to be very small, on the order of one tenth of a percent. This suggests that the error due to this approximation is at least an order of magnitude smaller than the amplitude of anisotropy computed here.

To create Fig. 3, the average perturbations over the second and third layer of the models are calculated for each azimuth to infer the velocity variations with azimuth in the crust (Fig. 3 a, b) and the average perturbations over layers four to six are used to plot velocity variations with azimuth in the upper-most mantle (Fig. 3 c, d). Imaged anisotropy is 180° periodic, but plotted for the full range of 360° in Fig. 3 for clarity. The sinusoid-like distributions in Fig. 3 do not average at 0 because they are plotted with respect to an isotropic background V_s model that was chosen a priori.

Supplementary Discussion

1. Comparisons with other data

In the tomographic images, isotropic anomalies show velocities generally higher in the Aegean Sea compared to the surrounding land (Fig. 2). Relatively low velocities are observed near where the NAF enters the Aegean Sea. Phase velocity anomalies we observe are influenced by variations in the Moho depth; the isotropic anomalies in the tomography reflect the thick crust beneath the Aegean forearc and the Hellenides. High velocities in the Aegean and Ionian Seas point to a shallower Moho there. These observations are in agreement with other tomographic studies of the area – from global to regional scale – based on body waves^{48,49,66,67} as well as surface waves^{61–65}. Observed Moho depth variations also agree with results from active seismics^{68,69}, receiver functions^{47,70,71} and gravity inversion¹².

Azimuthal anisotropy shows clearly different patterns at 15 and 30 s. Coherence analysis shows only minor variations between 12 s, 15 s, and 18 s maps. Anisotropy patterns rotate between 18 s and 25 s, but between 25 and 30 s the orientation is, again, stable. The occurrence of two period ranges with consistent anisotropy patterns is consistent with the presence of two depth ranges (lower crust and lithospheric mantle) with consistent orientations of azimuthal anisotropy.

The isotropic as well as anisotropic patterns at 25–30 s periods are consistent with the results of recent anisotropic Pn tomography⁷⁶ that sampled P-wave velocities and fast directions of P-wave anisotropy in the sub-Moho mantle (Supplementary Fig. 12). Negative isotropic anomalies mark the forearc along central western Greece, as well as the north-central Aegean (38–40°N, 24–26°E). Positive anomalies are located in the southern Aegean and along the Eastern and Western margins of continental Greece. The belt of velocities 10–15% below average along the forearc outlines a wedge of low velocities above the slab. The Pn anisotropic directions are described in ref. 76 as showing arc-parallel orientation along the Hellenic arc and

generally N-S orientation in the Aegean Sea. The smallest amount of anisotropy is observed in the Sea of Crete. This is consistent with our phase-velocity tomography at 30 s period that shows a clear N-S orientation in the northern part of the Aegean and continental Greece. The smallest amplitudes of anisotropy are also observed in the Sea of Crete.

SKS splitting measurements provide an important constraint on anisotropy in the Aegean and have been interpreted in a number of studies^{16,21,29,30}. The fast-propagation direction inferred from SKS splitting does not match the fast-propagation directions we find in the mantle lithosphere (Supplementary Fig. 13). However, SKS-inferred fast-propagation directions are nearly parallel to crustal fast-propagation directions in a part of the northern Aegean, with an average fast splitting direction of 38° at five stations (between 24°E and 27°E and 38°N and 42°N). The observed splitting time is, on average, 1.5 s. This is too large to be caused by crustal anisotropy alone as to create it, more than 15% of anisotropy within the crust (assuming a depth-independent distribution) would be required. This would result in amplitudes of up to 6.5% (at a period of 15 s) for azimuthal anisotropy in the tomographic inversion. Less than half of this amount is actually observed in the northern Aegean (on average 1.8%, with a maximum of 2.3%). This suggests that the splitting originates primarily below the lithosphere, probably in the asthenosphere.

2. Causes of the observed anisotropy

a) Anisotropy and strain in the northern Aegean mantle lithosphere

The fast directions of anisotropy in the northern Aegean lithospheric mantle match current directions of extension (Fig. 2). The current extensional strain field in this region has been active since about 5 m.y.¹¹, and strains on the order of 10^{-7} , as currently found in the northern Aegean^{15,16,21,41}, would produce finite strains of 0.5 over this time period. Calculations indicate that strain of 0.5 can result in 4 to 5% of shear wave anisotropy for a pure olivine aggregate deformed by uniaxial extension²⁵. This is larger than the observed values of approximately

3% for the uppermost mantle in the northern Aegean (Fig. 3), which does not consist of pure olivine, however. Numerical modeling indicates that complete reorientation of anisotropy by 90° requires a larger amount of strain^{28,77}, but reorientation of LPO already becomes apparent at finite strain of about 0.4⁷⁸. A comparison to anisotropy measured in a tectonically active region also suggests that finite strain values around 0.5 are sufficient to cause a measurable reorientation of LPO⁷⁹. From comparison with the orientation of the Miocene strain field, the reorientation of strain observed in the northern Aegean is likely to be around 30° , and might, thus, require less finite strain than needed for a complete 90° reorientation. A partially completed reorientation of anisotropy is also consistent with the observation of a smaller amount of anisotropy, compared to the numerical predictions²⁵.

b) Possible influence of subduction-related fluids on anisotropy

Only a small amount of anisotropy is found in the lithospheric mantle beneath the south-central Aegean (the Cyclades). This part of the region currently acts as a nearly non-deforming block, but strong extension did occur in this area in the Miocene (Fig. 2). Any previously existing fabric in 40–60 km depth must thus have been weakened. One possible mechanism for this is the interaction with subduction-related fluids, as the southern Cyclades form part of the volcanic arc of the Hellenic Subduction Zone, where seismological and petrogenic data suggest a fraction of 15–20% partial melt in the mantle wedge⁶⁵, and the Sea of Crete is located in a fore-arc region, for which fluid release into the mantle wedge due to phase transitions in the rocks of the subducting slab is expected. The presence of oriented melt pockets has been shown to weaken mineral alignment by diffusion creep and grain-boundary sliding⁸⁰ and, depending on orientation, overprint the anisotropy of the background medium⁸¹. Segregation of melt⁸⁰ or alignment of dykes with foliation⁸², which leads to a different orientation or a strengthening of anisotropy, respectively, is not supported by our data for the Aegean volcanic arc. Hydration at mantle stresses and temperatures below 1000–1100 K also leads to the activation of diffusion

creep instead of dislocation creep mechanisms for the deformation of olivine⁸³. The resulting B-type fabric shows an anisotropic fast axis orientation nearly perpendicular to the flow direction⁸⁴ and accordingly can result in trench-parallel anisotropy in the shallow portions of the mantle wedge^{85,86}. Modelling indicates that in back-arc direction, this trench-parallel anisotropy can be followed by a region of small anisotropy of varying direction indicating the transition from hydrous to anhydrous mantle⁷⁸, comparable to our observations in the Aegean mantle wedge. Lithospheric thinning accompanied by asthenospheric upwelling might also have played a role in weakening pre-existing anisotropic fabric.

c) Crustal anisotropy

Crustal anisotropy may be caused by the alignment of a number of minerals^{44,87,88} or, primarily in the upper crust, by fluid-filled microcracks^{89,90}. These processes are characterized by different time scales, with development of anisotropic fabric occurring over millions of years (and depending on thermal conditions⁹¹), whereas crack propagation and healing are nearly instantaneous in comparison.

Anisotropy related to fluid-filled cracks is caused by stress-alignment, i.e. large-scale regional stresses preferentially closing cracks and pore space that strikes perpendicular to the direction of maximum compressive stress⁸⁷. The resulting fast polarization direction is then parallel to the maximum compressive stress, as was observed in laboratory measurements^{92–94} and confirmed by numerical calculations⁹⁵. The distribution of aligned inclusions accordingly gives rise to extensive-dilatancy anisotropy⁸⁹. Stress-aligned cracks have been invoked, for example, to explain the crustal anisotropy patterns along the Cascadia subduction zone^{90,96} and in Japan⁹⁷. Most of these data refer to the upper crust, but in a subduction zone environment, fluid-filled cracks may also exist at larger depth^{98,99}. Comparison of our crustal anisotropy data with the direction of compressive strain from the Global Strain Rate Model⁴¹ and the principal axes of stress in the upper 30 km of the Earth from the World Stress Map¹⁰⁰ does not show any

correlation, however, especially not in the southern-central Aegean on which our interpretation of lower crustal anisotropy is focussed (Supplementary Fig. 14).

Lattice preferred orientation (LPO) in the lower crust can be created by plastic or viscous flow, with the preferred slip direction of the minerals oriented parallel to the flow lines⁸⁸. LPO can also play a role in upper and mid-crustal regions in metamorphic terranes¹⁰¹. While single lower-crustal minerals are highly anisotropic, the effects of their alignment may partially cancel each other in a rock consisting of various minerals⁸⁷, because the orientation of fast axes is not the same for different minerals within the same deformation field. At least for mica and amphibole, however, anisotropy effects add constructively⁸⁷ and these minerals tend to align with the fast axes parallel to foliation. Ductile flow in the lower crust in response to extension in the Aegean region is indicated by the exhumation of MCCs in the Cyclades and elsewhere in the Aegean Sea region¹⁰² and considered the reason for the relatively flat Moho in the Aegean, in spite of varying amounts of extension¹⁰³. Studies of microseismicity around the Aegean^{104–107} and in the central volcanic arc¹⁰⁸ indicate a ductile state of the present crust below 10 to 20 km¹⁰⁹. The observed anisotropy is likely to be caused by mineral alignment in the lower crust due to ductile flow, as has been suggested previously for crustal anisotropy in the Basin and Range province^{37,110,111}—a region with a similar extensional history and a similarly flat Moho.

Supplementary References

51. Gung, Y., Panning, M. & Romanowicz, B. Global anisotropy and the thickness of continents. *Nature* **422**, 707-711 (2003).
52. Smith, D. B., Ritzwoller, M. H. & Shapiro, N. M. Stratification of anisotropy in the Pacific upper mantle. *J. Geophys. Res.* **109**, B11309 (2004).
53. Sebai, A., Stutzmann, E., Montagner, J.-P., Sicilia, D. & Beucler, E. Anisotropic structure of the African upper mantle from Rayleigh and Love wave tomography. *Phys. Earth Planet. Int.* **155**, 48-62 (2006).

54. Lin, F.-C., Ritzwoller, M. H. & Snieder, R. Eikonal tomography: surface wave tomography by phase front tracking across a regional broad-band seismic array. *Geophys. J. Int.* **177**, 1091-1110 (2009).
55. Smith, M. L. & Dahlen, F. A. The azimuthal dependence of Love and Rayleigh wave propagation in a slightly anisotropic medium. *J. Geophys. Res.* **78**, 3321-3333 (1973).
56. Tanimoto, T. Free oscillations of a slightly anisotropic earth. *Geophys. J. R. astr. Soc.* **87**, 493-517 (1986).
57. Montagner, J.-P. & Anderson, D. L. Petrological constraints on seismic anisotropy. *Physics Earth Planet. Int.* **54**, 82-105 (1989).
58. Erduran, M., Endrun, B. & Meier, T. Continental vs. oceanic lithosphere beneath the eastern Mediterranean Sea - Implications from Rayleigh wave dispersion measurements. *Tectonophysics* **457**, 45-52 (2008).
59. Pedersen, H. A. Impacts of non-plane waves on two-station measurements of phase velocities. *Geophys. J. Int.* **165**, 279-287 (2006).
60. Sambridge, M. Geophysical inversion with a neighbourhood algorithm - I. Searching a parameter space. *Geophys. J. Int.* **138**, 479-494 (1999).
61. Martínez, M. D., Lana, X., Canas, J. A., Badal, J. & Pujades, L. Shear-wave velocity tomography of the lithosphere–asthenosphere system beneath the Mediterranean area. *Phys. Earth. Planet. Int.* **122**, 33-54 (2000).
62. Marone, F., van der Lee, S. & Giardini, D. Three-dimensional upper-mantle S-velocity model for the Eurasia–Africa plate boundary region. *Geophys. J. Int.* **158**, 109-130 (2004).

63. Bourova, E., et al. Constraints on absolute S velocities beneath the Aegean Sea from surface wave analysis. *Geophys. J. Int.* **160**, 1006-1019 (2005).
64. Karagianni, E. E., et al. Shear velocity structure in the Aegean area obtained by inversion of Rayleigh waves. *Geophys. J. Int.* **160**, 127-143 (2005).
65. Karagianni, E. E. & Papazachos, C. B. Shear velocity structure in the Aegean region obtained by joint inversion of Rayleigh and Love waves. in *The Geodynamics of the Aegean and Anatolia* (eds. Taymaz, T., Yilmaz, Y. & Dilek, Y.) 159-181 (Geol. Soc. Spec. Publ. Vol. 291, London, 2007).
66. Papazachos, C. & Nolet, G. P and S deep velocity structure of the Hellenic area obtained by robust nonlinear inversion of travel times. *J. Geophys. Res.* **102**, 8349-8367 (1997).
67. Drakatos, G., Karantonis, G. & Stavrakakis, G. N. P-wave crustal tomography of Greece with use of an accurate two-point ray tracer. *Ann. Geof.* **XL**, 25-36 (1997).
68. Makris, J. The crust and upper mantle of the Aegean region from deep seismic soundings. *Tectonophysics* **46**, 269-284 (1978).
69. Bohnhoff, M., Makris, J., Papanikolaou, D. & Stavrakakis, G. Crustal investigation of the Hellenic subduction zone using wide aperture seismic data. *Tectonophysics* **343**, 239-262 (2001).
70. Li, X., et al. Receiver function study of the Hellenic subduction zone: imaging crustal thickness variations and the oceanic Moho of the descending African lithosphere. *Geophys. J. Int.* **155**, 733-748 (2003).
71. Sodoudi, F., et al. Lithospheric structure of the Aegean obtained from P and S receiver functions. *J. geophys. Res.* **111**, B12307 (2006).

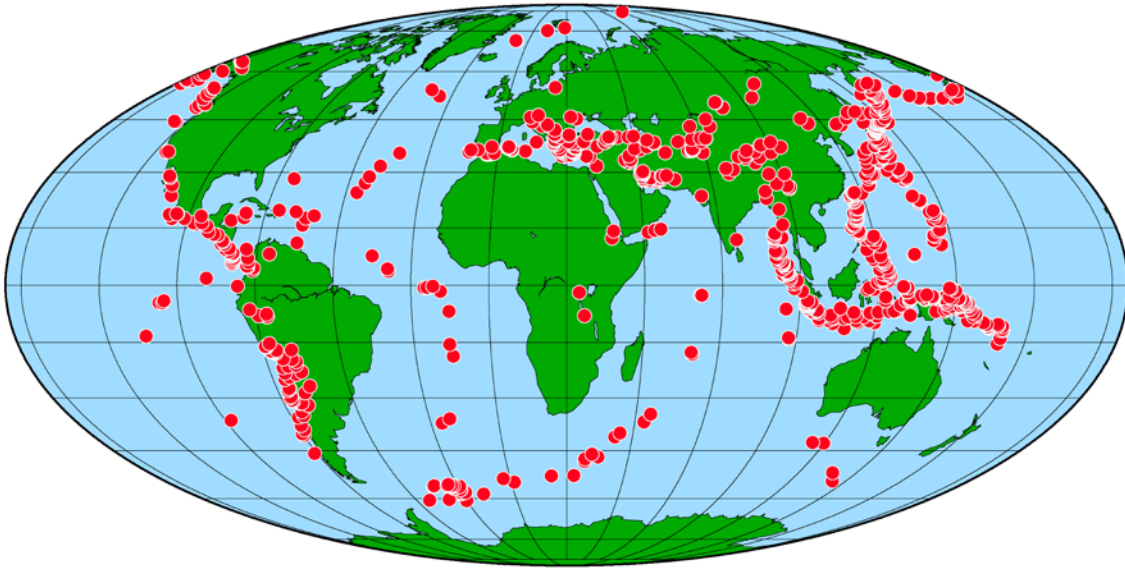
72. Griot, D.-A., Montagner, J.-P. & Tapponier, P. Confrontation of mantle seismic anisotropy with two extreme models of strain, in central Asia. *Geophys. Res. Lett.* **25**, 1447-1450 (1998).
73. Papazachos, B.C. & Comninakis, P.E. Geophysical and tectonic features of the Aegean arc. *J. geophys. Res.* **76**, 8517-8533 (1971).
74. Delibasis, N.D. Seismic wave attenuation in the upper Mantle beneath the Aegean region. *Pure appl. geophys.* **120**, 820-839 (1982).
75. Visser, K., Trampert, J., Lebedev, S. & Kennett, B. L. N. Probability of radial anisotropy in the deep mantle. *Earth Planet. Sci. Lett.* **270**, 241-250 (2008).
76. Al-Lazki, A. I., et al. Pn tomographic imaging of mantle lid velocity and anisotropy at the junction of the Arabian, Eurasian and African plates. *Geophys. J. Int.* **158**, 1024-1040 (2004).
77. Becker, T. W., Kellogg, J. B., Ekström, G. & O'Connell, R. J. Comparison of azimuthal seismic anisotropy from surface waves and finite strain from global mantle-circulation models. *Geophys. J. Int.* **155**, 696-714 (2003).
78. Lassak, T. M., Fouch, M. J., Hall, C. E. & Kaminski, E. Seismic characterization of mantle flow in subduction systems: Can we resolve a hydrated mantle wedge? *Earth Planet. Sci. Lett.* **243**, 632-649 (2006).
79. Becker, T. W., Schulte-Pelkum, V., Blackman, D. K., Kellogg, J. B. & O'Connell, R. J. Mantle flow under the western United States from shear wave splitting. *Earth Planet. Sci. Lett.* **247**, 235-251 (2006).
80. Holtzman, B. K., et al. Melt segregation and strain partitioning: Implications for seismic anisotropy and mantle flow. *Science* **301**, 1227-1230 (2003).

81. Mainprice, D. Modelling the anisotropic seismic properties of partially molten rocks found at mid-ocean ridges. *Tectonophysics* **279**, 161-179 (1997).
82. Tommasi, A., Vauchez, A., Godard, M. & Belley, F. Deformation and melt transport in a highly depleted peridotite massif from the Canadian Cordillera: Implications to seismic anisotropy above subduction zones. *Earth Planet. Sci. Lett.* **252**, 245-259 (2006).
83. Katayama, I. & Karato, S. Effect of temperature on the B- to C-type fabric transition in olivine. *Phys. Earth Planet. Int.* **157**, 33-45 (2006).
84. Jung, H. & Karato, S. Water-induced fabric transitions in olivine. *Science* **293**, 1460-1463 (2001).
85. Mizukami, T., Wallis, S. R. & Yamamoto, J. Natural examples of olivine lattice preferred orientation patterns with a flow-normal a-axis maximum. *Nature* **427**, 432-436 (2004).
86. Kneller, E. A., van Keken, P. E., Katayama, I. & Karato, S. Stress, strain, and B-type olivine fabric in the fore-arc mantle: Sensitivity tests using high-resolution steady-state subduction zone models. *J. Geophys. Res.* **112**, B04406 (2007).
87. Barruol, G. & Mainprice, D. 3-D seismic velocities calculated from lattice-preferred orientation and reflectivity of a lower crustal section: examples of the Val Sesia section (Ivrea zone, northern Italy). *Geophys. J. Int.* **115**, 1169-1188 (1993).
88. Weiss, T., Siegesmund, S., Rabbel, W., Bohlen, T. & Pohl, M. Seismic velocities and anisotropy of the lower continental crust: A review. *Pure Appl. Geophys.* **156**, 97-122 (1999).
89. Crampin, S. & Lovell, J. H. A decade of shear-wave splitting in the Earth's crust: what does it mean? what use can we make of it? and what should we do next? *Geophys. J. Int.* **107**, 387-407 (1991).

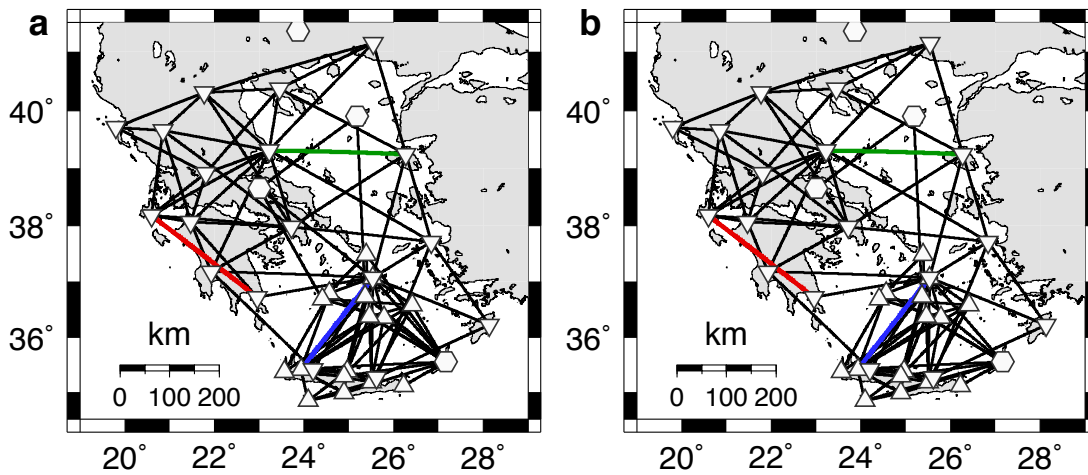
90. Currie, C. A., Cassidy, J. F. & Hyndman, R. D. A regional study of shear wave splitting above the Cascadia Subduction Zone: Margin-parallel crustal stress. *Geophys. Res. Lett.* **28**, 659-662 (2001).
91. Savage, M. K. Seismic anisotropy and mantle deformation in the western United States and southwestern Canada. *Int. Geol. Rev.* **44**, 913-937 (2002).
92. Nur, A. & Simmons, G. Stress-induced velocity anisotropy in rock: An experimental study. *J. Geophys. Res.* **74**, 6667-6674 (1969).
93. Birch, F. The velocity of compressional waves in rocks to 10 kilobars, part 2. *J. Geophys. Res.* **66**, 2199-2224 (1961).
94. Christensen, N. I. Shear wave velocities in metamorphic rocks at pressures to 10 kilobars. *J. Geophys. Res.* **71**, 3549-3556 (1966).
95. Crampin, S. Effective anisotropic elastic constants for wave propagation through cracked solids. *Geophys. J. R. astr. Soc.* **76**, 135-145 (1984).
96. Cassidy, J. F. & Bostock, M. G. Shear-wave splitting above the subducting Juan de Fuca plate. *Geophys. Res. Lett.* **23**, 941-944 (1996).
97. Kaneshima, S. & Ando, M. An analysis of split shear waves observed above crustal and uppermost mantle earthquakes beneath Shikoku, Japan: Implications in effective depth extent of seismic anisotropy. *J. Geophys. Res.* **94**, 14077-14092 (1989).
98. Iidaka, T. & Obara, K. Shear-wave polarization anisotropy in the mantle wedge above the subducting Pacific plate. *Tectonophysics* **249**, 53-68 (1995).
99. Healy, D., Reddy, S. M., Timms, N. E., Gray, E. M. & Vitale Brovarone, A. Trench-parallel fast axes of seismic anisotropy due to fluid-filled cracks in subducting slabs. *Earth Planet. Sci. Lett.* **283**, 75-86 (2009).

100. Heidbach, O., et al. Stress maps in a minute: The 2004 World Stress Map release. *Eos Trans. AGU* **85**, 521 (2004).
101. Christensen, N. I. & Mooney, W. D. Seismic velocity structure and composition of the continental crust: A global view. *J. Geophys. Res.* **100**, 9761-9788 (1995).
102. Jolivet, L., Faccenna, C., Goffé, B., Burov, E. & Agard, P. Subduction tectonics and exhumation of high-pressure metamorphic rocks in the Mediterranean orogens. *Am. J. Sci.* **303**, 353-409 (2003).
103. Avigad, D., Baer, G. & Heimann, A. Block rotations and continental extension in the central Aegean Sea: palaeomagnetic and structural evidence from Tinos and Mykonos (Cyclades, Greece). *Earth Planet. Sci. Lett.* **157**, 23-40 (1998).
104. King, G. C. P., et al. The evolution of the Gulf of Corinth (Greece): an aftershock study of the 1981 earthquakes. *Geophys. J. R. astr. Soc.* **80**, 677-693 (1985).
105. Eyidoğan, H. & Jackson, J. A seismological study of normal faulting in the Demirci, Alaşehir and Gediz earthquakes of 1969-70 in western Turkey: implications for the nature and geometry of deformation in the continental crust. *Geophys. J. R. astr. Soc.* **81**, 569-607 (1985).
106. Rigo, A., et al. A microseismic study in the western part of the Gulf of Corinth (Greece): implications for large-scale normal faulting mechanisms. *Geophys. J. Int.* **126**, 663-688 (1996).
107. Meier, T., Rische, M., Endrun, B., Vafidis, A. & Harjes, H.-P. Seismicity of the Hellenic subduction zone in the area of western and central Crete observed by temporary local seismic networks. *Tectonophysics* **383**, 149-169 (2004).

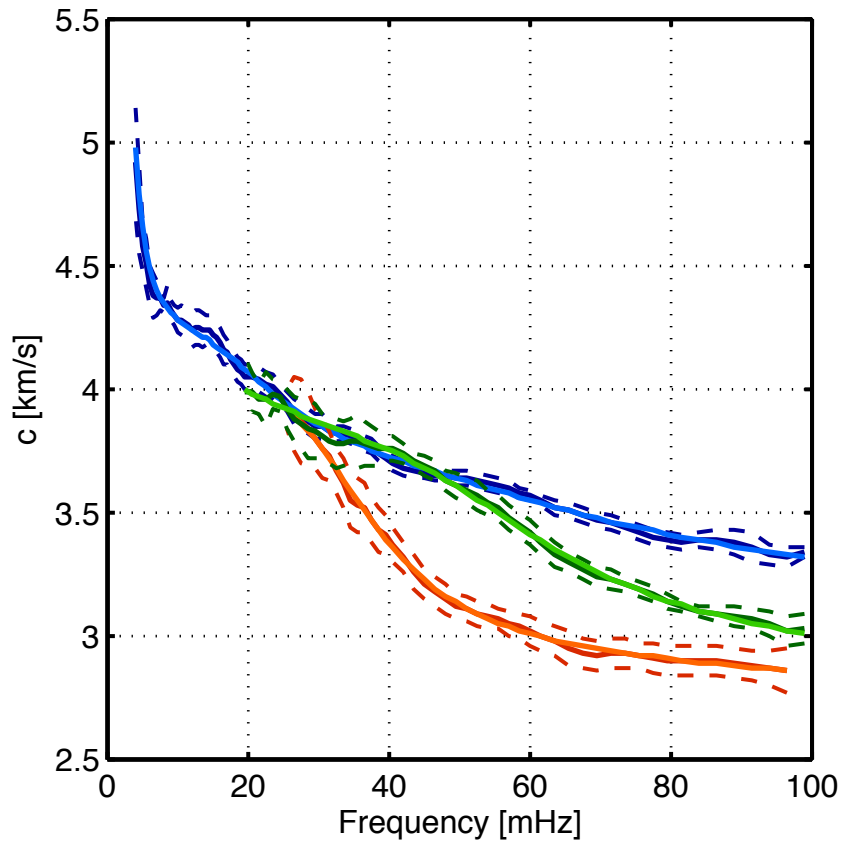
108. Bohnhoff, M., et al. Microseismic activity in the Hellenic Volcanic Arc, Greece, with emphasis on the seismotectonic setting of the Santorini-Amorgos zone. *Tectonophysics* **423**, 17-33 (2006).
109. Jolivet, L. & Patriat, M. Ductile extension and the formation of the Aegean Sea. In *The Mediterranean Basins: Tertiary Extension within the Alpine Orogen* (eds. Durand, B., Jolivet, L., Horváth, F. & Séranne, M.) 427-456 (Geol. Soc. Spec. Publ. Vol. 156, London, 1999).
110. Carbonell, R. & Smithson, S. B. Large-scale anisotropy within the crust in the Basin and Range Province. *Geology* **19**, 698-701 (1991).
111. McNamara, D. E. & Owens, T. J. Azimuthal shear wave velocity anisotropy in the Basin and Range Province using Moho Ps converted phases. *J. Geophys. Res.* **98**, 12003-12017 (1993).



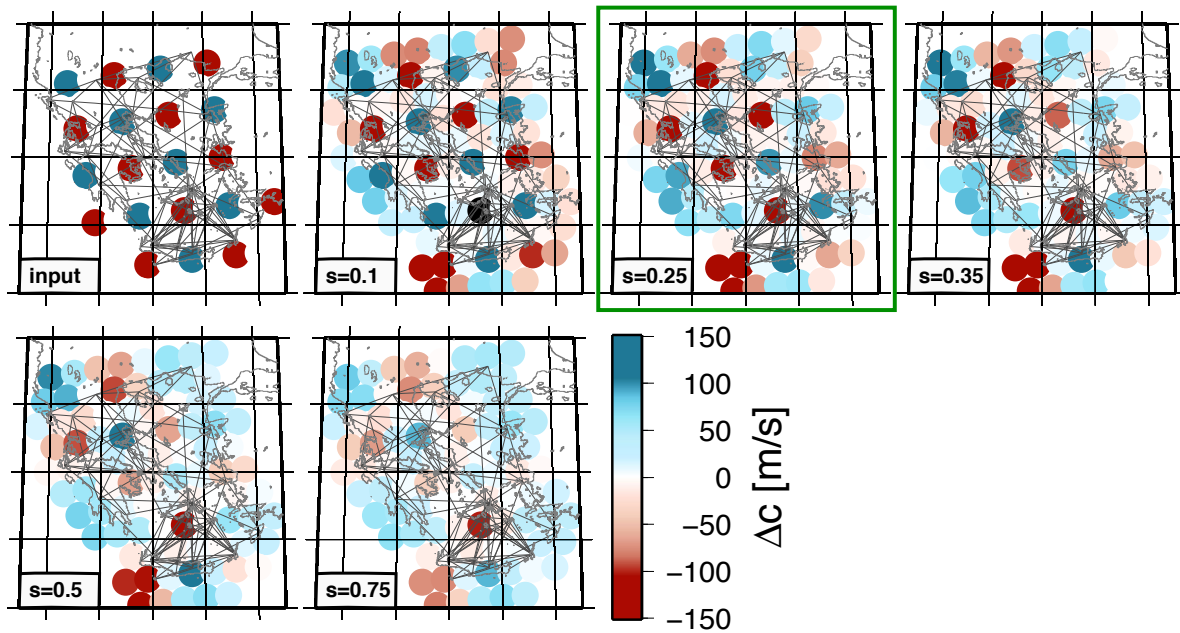
Supplementary Figure 1: Distribution of earthquakes used to measure interstation phase velocities.



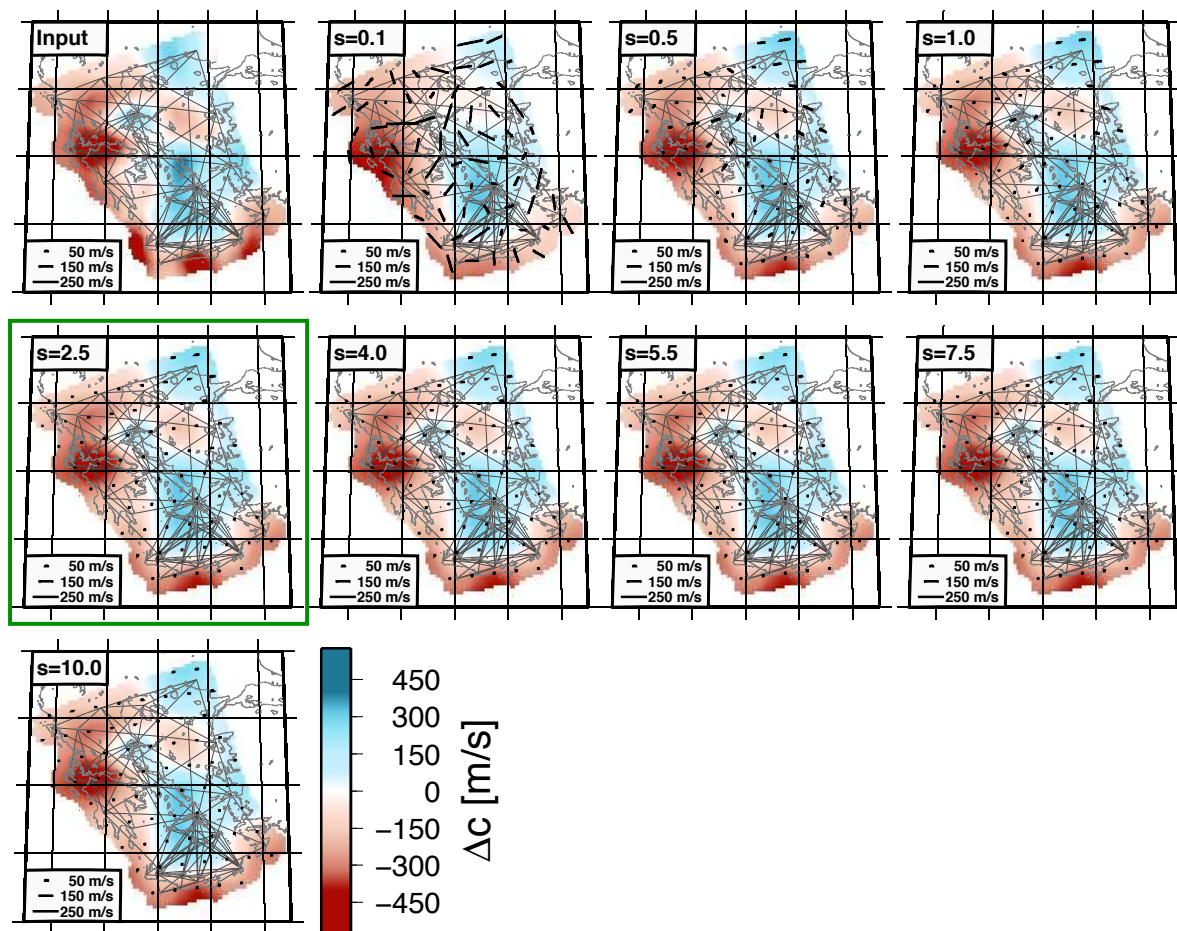
Supplementary Figure 2: Ray-path coverages at 15 s (a) and 30 s (b) period. Coloured ray paths correspond to the dispersion curves plotted in Supplementary Fig. 2 (same colours). Triangles denote STS-2 seismometers (GEOFON, MEDNET and temporary CYCNET networks), inverted triangles stand for Le-3D 20s sensors (NOA network) and hexagons for CMG-40T 30s seismometers (NOA network)⁴⁰.



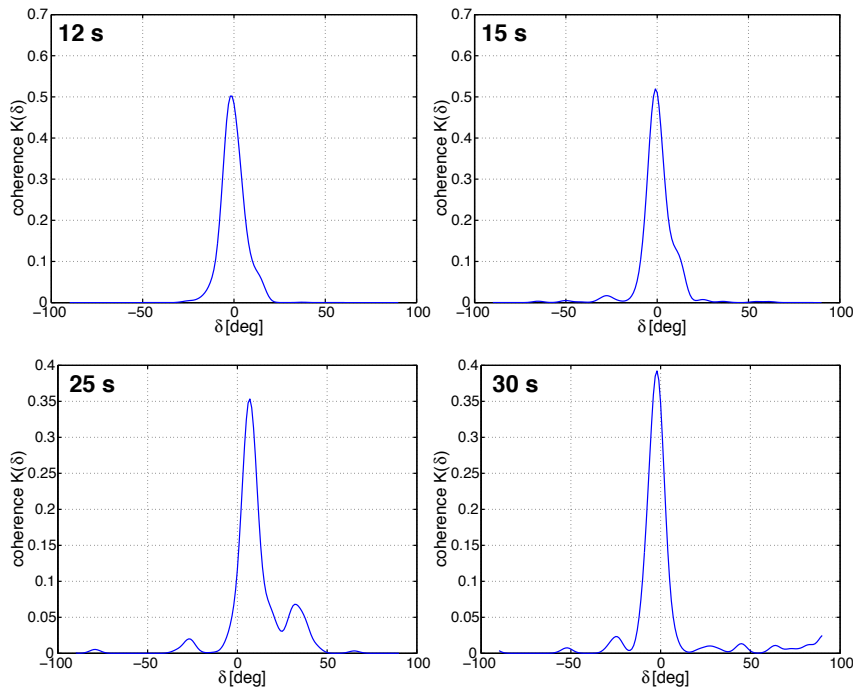
Supplementary Figure 3: Examples of dispersion curves used as input to the tomography. Darkly coloured curves are the originally measured ones with 99% confidence interval (dashed lines), while lighter curves represent the smoothed version used in the tomography. The example curves are from three different areas of the Aegean region (Supplementary Fig. 2): the forearc (red curve, Peloponnese), the Sea of Crete (blue curve, Crete to the Cyclades) and the backarc (green curve, the northern Aegean). Large differences in phase velocity at high frequencies between 50 and 100 Hz are due to differences in crustal shear velocities and Moho depths.



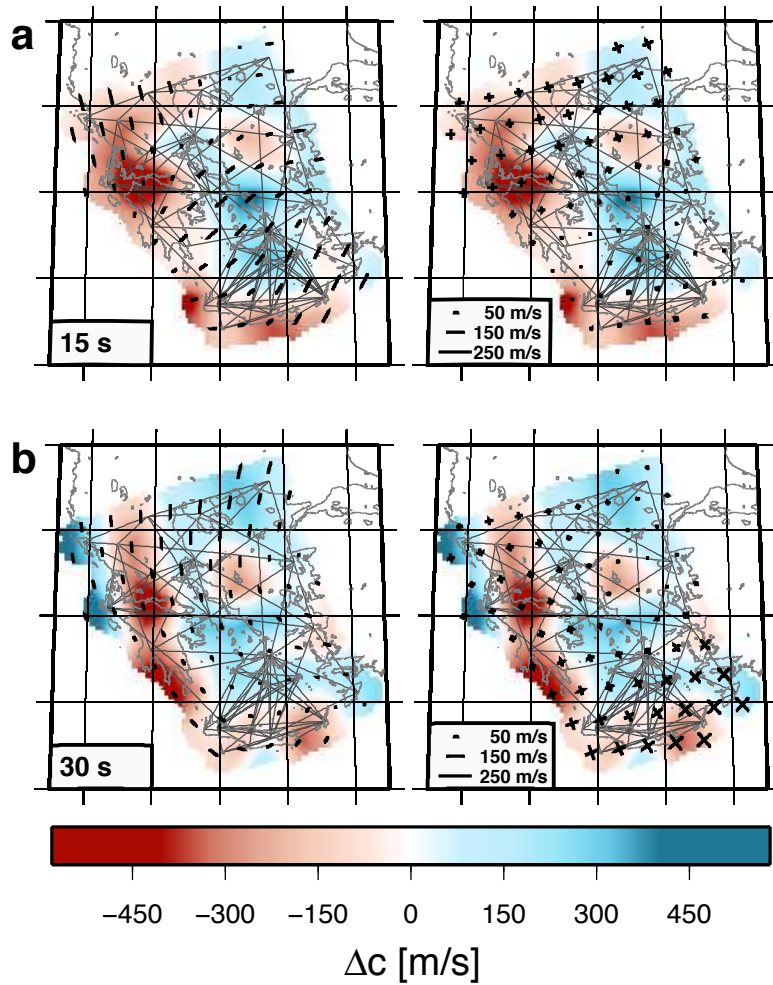
Supplementary Figure 4: Resolution tests conducted to determine the smoothing parameter for the isotropic part of the phase velocity maps at a period of 15 s. The input consists of a mixed spike-checkerboard pattern, and the output of the tomography is shown for different values of the smoothing parameter s for a reference average Rayleigh phase velocity of 3.24 km/s. Dark grey lines indicate the ray-path coverage. The black circle in the result for $s = 0.1$ indicates an amplitude outside the range of the colourbar, i.e. larger than in the input data. Ideally, the input should be recovered fully without any smearing or amplitude degradation. As this is not possible, however, especially at the boundaries of the region which are not well covered by crossing rays, the value of s associated with the most faithful recovery of the input ($s = 0.25$, green frame) is chosen. Note that the regions at the periphery of the study area that show poor resolution are not displayed or used in the interpretation of the data (Fig. 2).



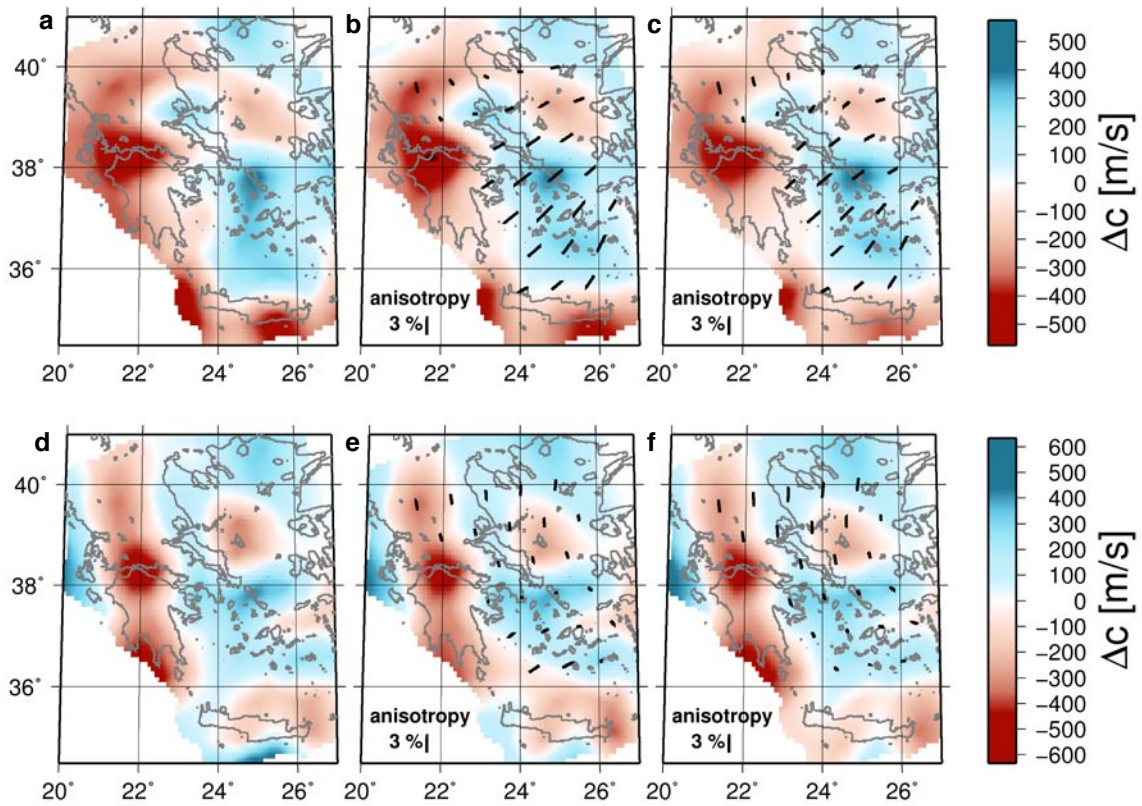
Supplementary Figure 5: Resolution tests used to determine the smoothing parameter for the 2Ψ anisotropic part of the phase velocity maps at a period of 15 s. The input consists of a purely isotropic part of the actual tomographic inversion at this period (3.24 km/s reference average Rayleigh phase velocity), and the output is shown for different values of the smoothing parameter s . Dark grey lines indicate the ray-path coverage. Ideally, the input should be recovered fully without any amplitude degradation and any spurious anisotropy (as no anisotropy is contained in the input). The choice of s ($s = 2.5$, green frame) is motivated by the lack of visible reduction in spurious anisotropy (black bars) for larger values of s . Some degradation of amplitudes in the isotropic part, especially near the borders of the region, where coverage and resolution is insufficient (i.e. in the south-western and south-eastern corners of the covered region) is evident for all values of s , but the main patterns are faithfully recovered. Note that the regions near the boundaries of the study area that show poor resolution are not displayed or used in the interpretation of the data (Fig. 2).



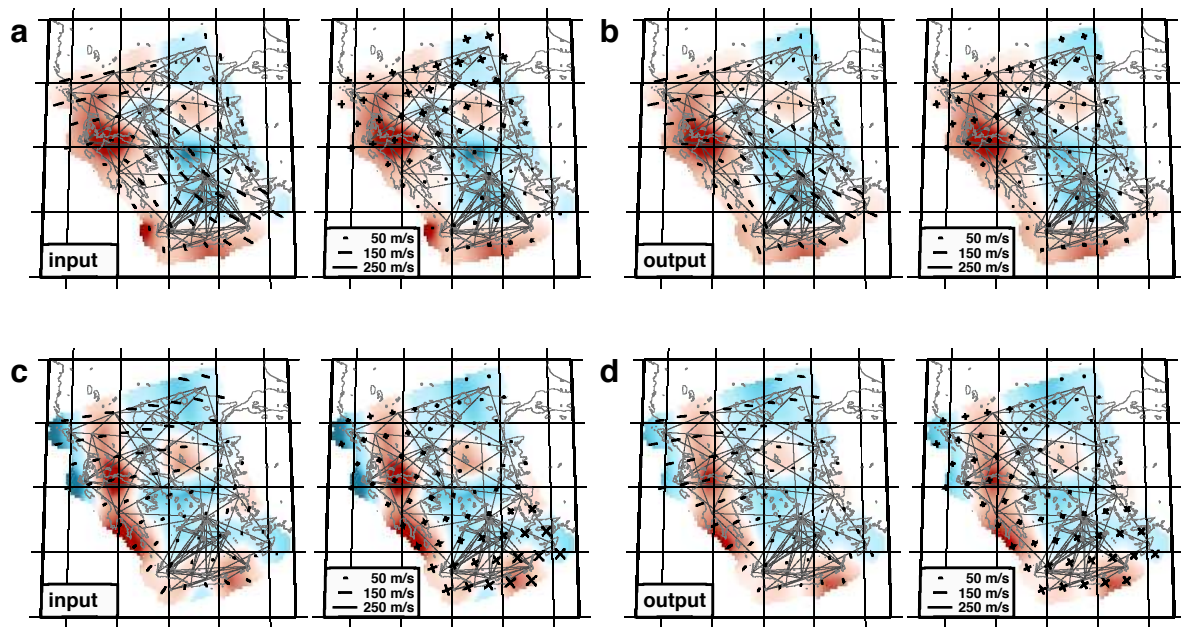
Supplementary Figure 6: Coherency function measuring the correlation between the orientation of 2Ψ anisotropy for inversions with and without 4Ψ terms at different periods. Values of δ at which the peak amplitudes occur indicate the rotation of 2Ψ anisotropy between the data sets, which is very small at periods of 12 s, 15 s and 30 s and also below 7° for 25 s.



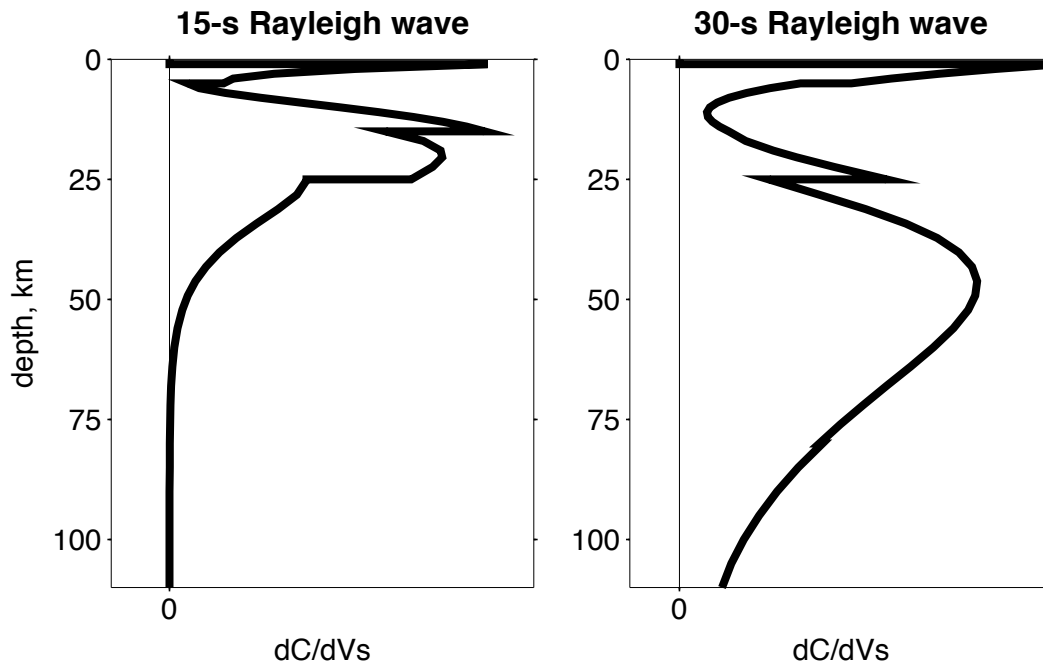
Supplementary Figure 7: Results of anisotropic tomography at 15 s (a) and 30 s (b) period including both 2Ψ (left) and 4Ψ (right) terms. Reference average Rayleigh phase velocities are 3.24 km/s (a) and 3.77 km/s (b).



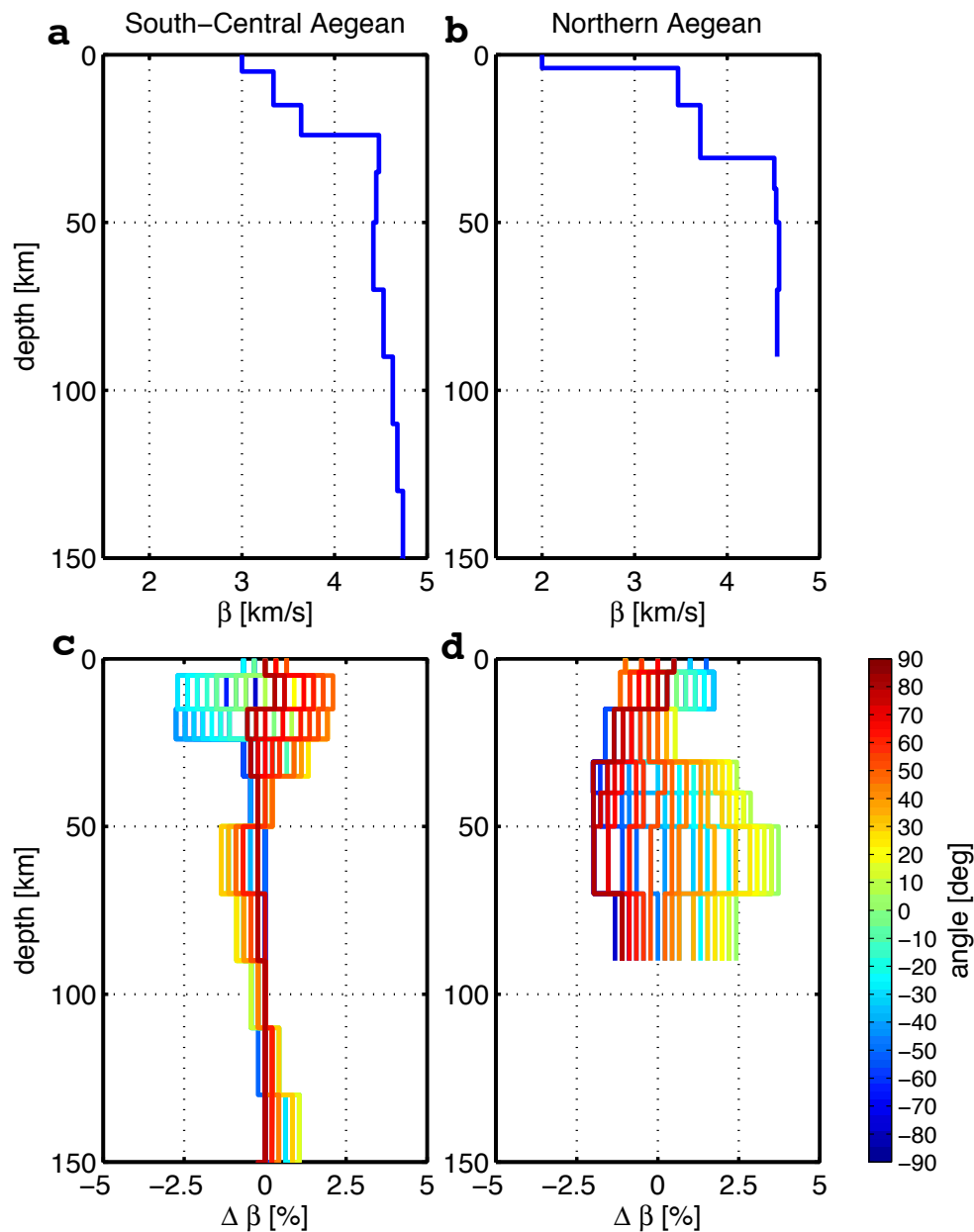
Supplementary Figure 8: Comparison of inversion results at 15 s (a — c) and 30 s (d — f) when allowing for isotropic perturbations only (a, d), including isotropic perturbations and 2Ψ anisotropic terms (b, e) and additionally allowing 4Ψ terms (c, f).



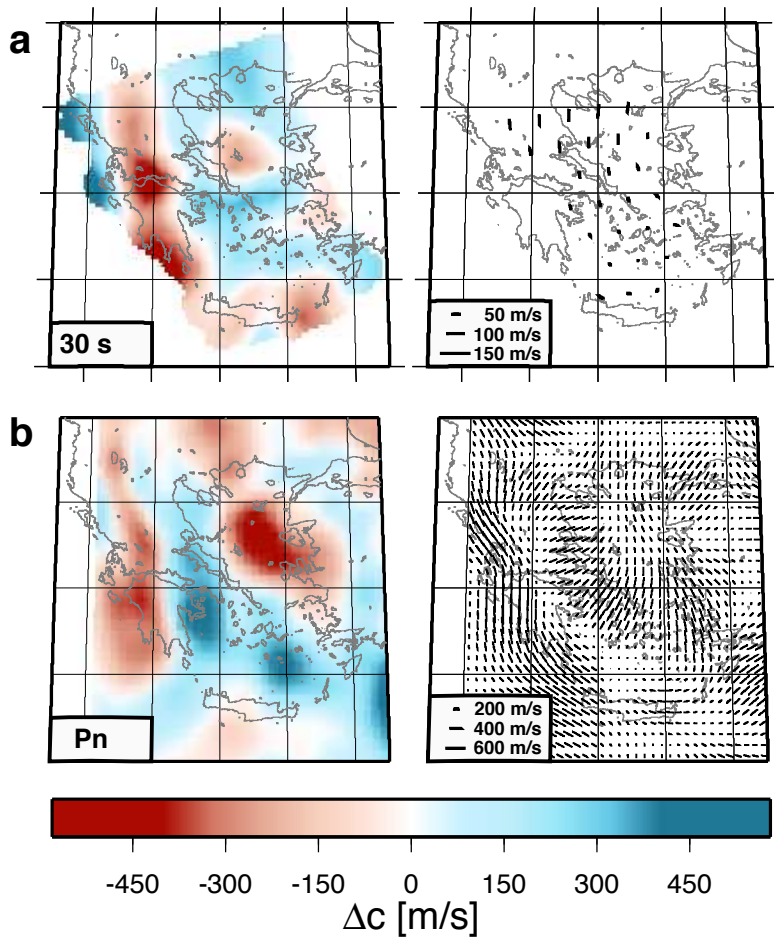
Supplementary Figure 9: Results of resolution test where the input includes the isotropic and 4Ψ terms as observed in the inversion of the data and the 2Ψ terms rotated by 90 deg. The input and recovered output are shown for periods of 15 s (a, b) and 30 s (c, d) with average Rayleigh phase velocities of 3.24 km/s (a,b) and 3.77 km/s (c,d).



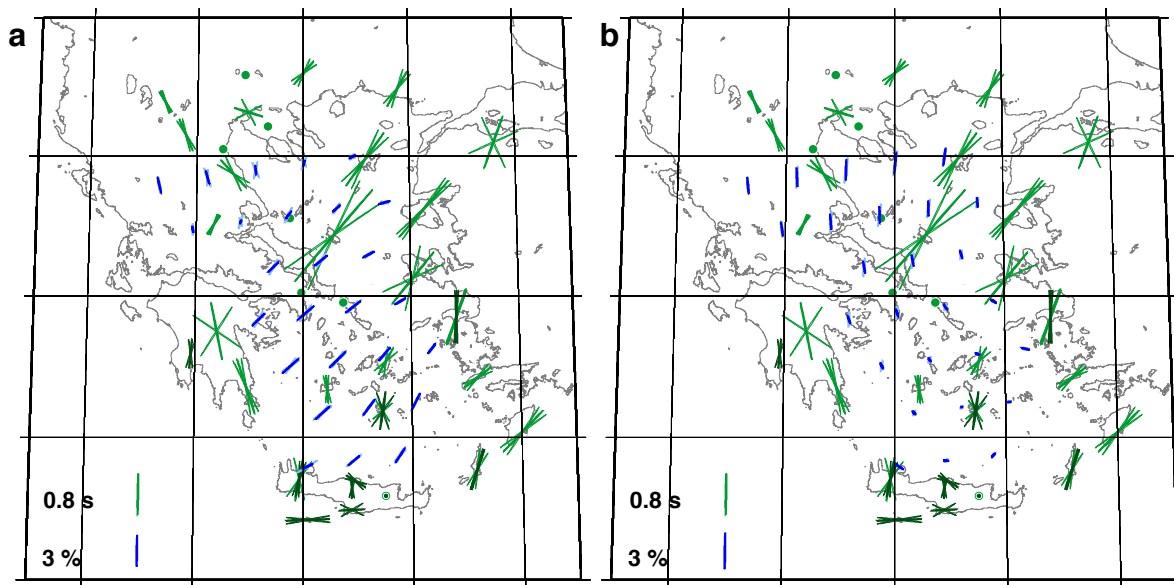
Supplementary Figure 10: Fréchet derivatives of the phase velocity of the fundamental Rayleigh mode with respect to S-wave velocities, at 15 and 30 s periods. Each graph is scaled independently. The derivatives are computed for a model with a 1-km water layer and a 25-km Moho depth.



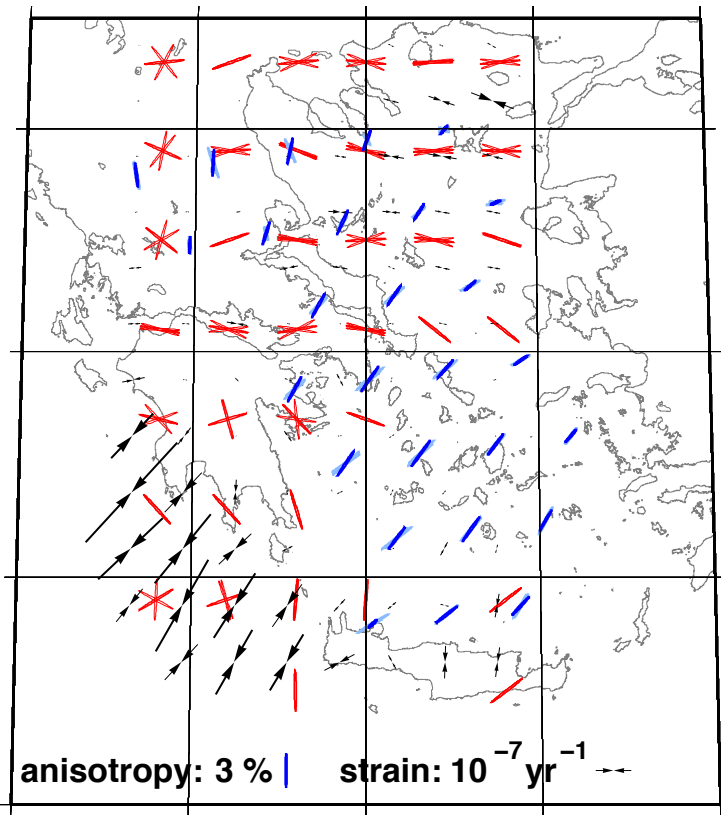
Supplementary Figure 11: a, b: Isotropic region-average V_s profiles obtained by gradient-search inversions of isotropic-average phase velocities derived from phase-velocity maps (e.g., Fig. 2) within the regions (south-central and northern Aegean). c, d: Azimuth-specific V_s profiles within the regions, plotted as perturbations to the isotropic-average profiles (a, b) vs. depth. Anisotropic perturbations were added to the phase velocity curves by projecting the average measured anisotropy in each of the regions on different azimuths in 5° steps. The resulting phase velocity curves were then independently inverted for shear-velocity models, using the background models as initial solution and keeping the depth of all layers fixed. The azimuthal variations of V_s in the crust and lithospheric mantle are summarized in Fig. 3.



Supplementary Figure 12: Comparison of the results of anisotropic surface wave tomography at 30 s period (a) with results of Pn tomography (b) of the region⁷⁶. Isotropic anomalies are plotted on the left side, using the same colour scale, a reference average Rayleigh phase velocity of 3.77 km/s (a) and a reference Pn velocity of 8.0 km/s (b), while azimuthal anisotropy is shown on the right side, using different scales as indicated.



Supplementary Figure 13: Comparison of fast-propagation directions inferred from SKS splitting studies (ref. 29 - light green bars, ref. 30 - dark green bars) with error estimates and fast axes of surface-wave anisotropy at two different periods: 15 s (a) and 30 s (b). Measurements at these periods are marked by dark blue bars, while measurements at adjacent periods of 12 and 18 s and 25 s, respectively, are outlined by light blue bars. No correlation is evident, except perhaps for crustal depth (12 - 18 s period) within the northern Aegean.



Supplementary Figure 14: Comparison of the fast axes of anisotropy in the lower crust (12–18 s period, blue) with principal directions of compression (black arrows) from the Global Strain Rate Map project⁴¹ as well as principal stress orientations from the World Stress Map¹⁰⁰ for the upper 30 km. Dark blue bars indicate the inversion results at 15 s, while lighter blue bars plotted below indicate the results for the adjacent periods of 12 s and 18 s. Little compression is evident in the central Aegean region which shows consistently NE-SW oriented anisotropy. In other regions (Crete, Gulf of Corinth, northern Aegean), where larger compressional strains are observed, they are not oriented parallel to the fast-propagation direction, as would be expected were anisotropy caused by stress-aligned cracks.